Eur. Radiol. (2001) 11: 884–892

EXPERIMENTAL

Elmar M. Merkle
Jason R. Shonk
Lan Zheng
Jeffrey L. Duerk
Jonathan S. Lewin

MR imaging-guided radiofrequency thermal ablation in the porcine brain at 0.2 T

Received: 7 February 2000
Revised: 18 July 2000
Accepted: 19 July 2000

E. M. Merkle · J. R. Shonk · J. L. Duerk · J. S. Lewin
Department of Radiology,
University Hospitals of Cleveland,
Case Western Reserve University,
11100 Euclid Avenue, Cleveland,
Ohio 44106, USA

E. M. Merkle (✉)
Department of Diagnostic Radiology,
University of Ulm, Robert Koch Street 8,
89081 Ulm, Germany
e-mail: elmar.merkle@medizin.uni-ulm.de
Tel.: + 49-731-5024863
Fax: + 49-731-5024703

L. Zheng · J. L. Duerk
Department of Biomedical Engineering,
Case Western Reserve University,
10900 Euclid Avenue, Cleveland,
Ohio 44106, USA

J. S. Lewin
Department of Oncology,
University Hospitals,
Case Western Reserve University,
11100 Euclid Avenue, Cleveland,
Ohio 44106, USA

Abstract The aim of this study was to test the hypotheses that (a) MR imaging-guided radiofrequency (RF) thermal ablation is safe and feasible in porcine brain using an open C-arm-shaped low-field MR system, and that (b) induced thermal lesion size can be predicted using low-field MR imaging. Magnetic resonance-guided RF ablation was performed in the cerebral frontal lobes of six pigs. An 18-G monopolar RF electrode was inserted into the porcine brain using MR image guidance and RF was then applied for 10 min. After post-procedure imaging (T2-weighted, T1-weighted before and after gadodiamide administration), the pigs were killed and the brains were used for pathologic examination. Successful RF electrode placement was accomplished in all cases without complications; total magnet time ranged from 73 to 189 min. The thermal lesion size varied from 10 to 12 mm perpendicular to the electrode track and was easily visualized on T2-weighted and enhanced T1-weighted images. Enhanced T1-weighted imaging demonstrated the highest brain-to-RF thermal lesion contrast-to-noise ratio with an average of 1.5 ± 1.6. Enhanced T1-weighted imaging never underestimated pathologic lesion diameter with a mean difference of 2.3 ± 1.0 mm and a radiologic/pathologic correlation of 0.69. Magnetic resonance imaging-guided RF thermal ablation is feasible and safe in the porcine brain using an open MR low-field system. Induced thermal lesion size can best be monitored using enhanced T1-weighted images. In the future, RF ablation under low-field MR guidance may offer an alternative treatment option for primary and secondary brain tumors.

Key words Brain, thermal ablation · Radiofrequency, MR · Experimental

Introduction

Minimally invasive treatment modalities for primary and secondary malignant brain tumors have become an area of considerable interest during the past few years. In addition to more common minimally invasive neurosurgical procedures, such as neuroendoscopy for intraventricular access, or transphenoidal endoscopic surgery for resection of pituitary tumors, minimally invasive methods for deposition of localized thermal energy can also be applied to destroy focal brain tumors. Thermal energy to induce coagulation necrosis can be delivered using many different energy sources, such as laser, cryotherapy, radiofrequency (RF), microwaves, or focused ultrasound [1, 2, 3, 4, 5, 6].

Magnetic resonance imaging with its high soft tissue contrast, multiplanar imaging capabilities, high spatial resolution, and temperature sensitivity, is well suited for monitoring temperature–tissue interactions. This had been proven in numerous ex vivo as well as in vivo brain studies [1, 2, 6, 7, 8, 9, 10, 11]. In all of these studies, however, MR imaging of the brain was performed using conventional cylindrical superconducting MR systems with a magnetic field strength of at least 1.5 T. Although conventional high-field systems offer excellent image quality, they have the disadvantage of limited patient access. We therefore sought to determine (a) whether MR imaging-guided RF thermal ablation is safe and feasible in the porcine brain using an open C-arm-shaped low-field MR system, and (b) if induced thermal lesion size can be predicted using low-field MR imaging.

Materials and methods

MR imaging system

Guidance of RF electrode insertion and monitoring of ablation were performed using a 0.2-T clinical C-arm MR imaging system (Siemens, Magnetom Open, Erlangen, Germany) with three modifications to facilitate image-guided interventions [12].

In the first modification, an in-room 1024 × 1280 pixel, RF-shielded, liquid crystal monitor was installed for image viewing at the side of the magnet, analogous to a fluoroscopic monitor. Secondly, control of the imager from within the imaging suite was made possible using an MR-compatible mouse and foot pedal. Thirdly, rapid gradient-echo sequences were applied (fast imaging with steady-state precession, FISP; TR/TE/NSA/flip angle: 17.8/8.1 ms/2/90°, acquisition time 8 s/3 images, slice thickness 5 mm, field of view (FOV) 188 × 250 mm, matrix 96 × 256) to produce images with clinically adequate signal-to-noise ratio and sufficient temporal as well as spatial resolution. The whole-body transmit coils incorporated in the scanner were used for RF transmission, and a circular polarized head coil was used for signal reception.

Animal model

Using an Institutional Animal Care and Use Committee approved protocol, each of six domestic farm pigs (females 20–25 kg) was anesthetized using a combination of acepromazine (0.25 mg/kg, Fermenta Animal Health Co., Kansas City, Mo.) and ketamine (7.5 mg/kg, Phoenix Scientific, St. Joseph, Mo.) by IM injection. A 20-G by 1-in. IV catheter (Terumo, Elkton, Md.) was then inserted in a dorsal ear vein, and pentothal was administered (15 mg/kg, Abbott Laboratories, North Chicago, Ill.) via IV injection to allow tracheal intubation. Mechanical ventilation was then used throughout the procedure, and anesthesia was maintained with repeated doses of pentothal. The animal's lateral hindquarters were shaved bilaterally, and one 8 × 12-cm wire-mesh grounding pad coated with conductive gel was placed on each limb. Each pig was positioned left side down within the gantry of the MR scanner to allow access to the skull through the open magnet and the circular polarized head coil.

RF ablation

An ablation site was chosen in the frontal lobe using axial T2-weighted turbo spin-echo images [TR/TE/NSA/echo train length (ETL): 2069/102 ms/4/7; acquisition time 3 min 40 s, slice thickness 6 mm, FOV 188 × 250 mm, matrix 182 × 256]. The electrode insertion site was localized on the skin surface relative to the target tissue using a fluid-filled syringe visualized on rapid successive axial FISP images, as mentioned previously (Fig. 1 a). Following incision of the skin and periostal layer, a single 5.6-mm burr hole was made using an MR-compatible manually driven, 4.5-G titanium drill (Minrad, Clarence, N.Y.), taking care not to breech the dura (Fig. 2). A custom-made MR-compatible, 18-G monopolar electrode with a 2-cm exposed tip (Radionics, Burlington, Mass.) was advanced under a continuous imaging mode which consisted of repeated acquisition, reconstruction, and display of a set of three parallel 5-mm FISP images, as noted previously (Fig. 1 b,c). This set of slices was centered on the predicted electrode path to allow rapid detection of electrode bending or deflection [12]. Following placement of the electrode at the target site, the position was confirmed using a T2-weighted turbo spin-echo sequence (TR/TE/NSA/ETL: 2000/105 ms/2/17; acquisition time 1 min 3 s/5 images, slice thickness 5 mm, FOV 199 × 265 mm, matrix 170 × 256; Fig. 1 d). This sequence was chosen to precisely confirm the electrode position prior to ablation because of the superiority of turbo spin-echo sequences over gradient-echo sequences in depicting accurate tip position [13]. For each ablation, RF was applied for 10 min using a 120-W RF generator operating at 500 kHz (modified model RFG-3C, Radionics, Burlington, Mass.) with the tip temperature maintained at 90 ± 2 °C. Impedance, current, and tip temperature were documented every 60 s during RF application. These values were recorded from the RF generator's built-in display. Post-procedure imaging included turbo spin-echo T2-weighted (TR/TE/NSA/ETL: 2000/105 ms/2/17; acquisition time 1 min 3 s/5 images, slice thickness 5 mm, FOV 199 × 265 mm, matrix 170 × 256) and spin-echo T1-weighted (TR/TE/NSA: 400/26/3; acquisition time 2 min 56 s/9 images, slice thickness 5 mm, FOV 188 × 250 mm, matrix 144 × 256) sequences. T1-weighted images were repeated following the intravenous administration of 0.2 mmol/kg gadodiamide (Omniscan, Nycomed, Princeton, N.J.). Images were obtained in axial and coronal scan planes. These sequences were chosen based on prior work which demonstrated the usefulness of T2-weighted and T1-weighted images for visualization of thermally induced lesions [7, 14, 15].

All ablation procedures were evaluated in terms of time and success. The animals were killed using an overdose of IV pentothal, and all brains were used for gross pathological and histological examination. The formalin-fixed brains were cut either in the frontal plane parallel to the electrode track or in the horizontal plane perpendicular to the track. After photographic documentation, all slices which contained the RF thermal lesion were embedded in paraffin, and 6-μm-thick sections of each block were serially cut and stained with hematoxylin and eosin, and Masson's trichrome. The maximum diameter of each coagulative lesion was measured perpendicular to the RF electrode tract on post-procedure images using electronic calipers on the workstation monitor. Imaged dimensions were compared with those obtained at gross pathology.

Image analysis

Signal amplitude of the image background (noise), the RF thermal lesion, and the uninvolved contralateral frontal lobe were measured for each post-RF sequence by defining regions of interest

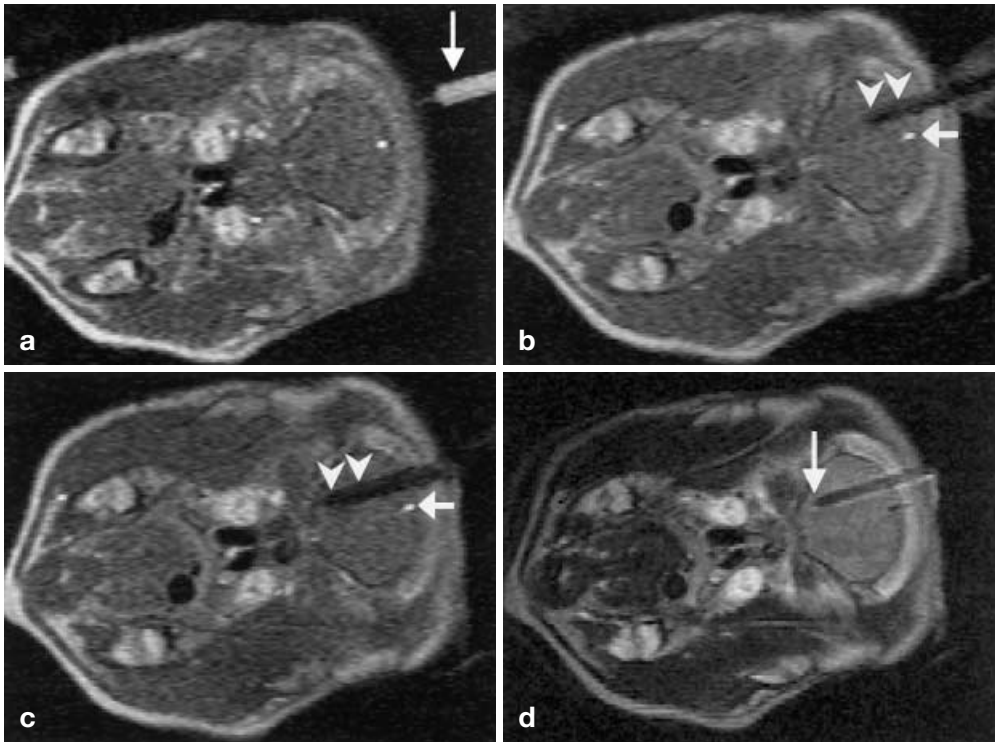

Fig. 1 a–d Localization of skull burr hole site and insertion of 18-G MR compatible RF electrode into right cerebral frontal lobe of a domestic farm pig. **a** With fluid-filled syringe *(arrow)*, puncture site on skull surface can be easily localized on axial gradient-echo T1-weighted images (fast imaging with steady-state precession, FISP; TR/TE/no. of excitations/flip angle 17.8/8.1 ms/1/90°). **b,c** Axial gradient-echo T1-weighted images FISP (TR/TE/no. of excitations/flip angle 17.8/8.1 ms/1/90°) show insertion of the MR-compatible 18-G RF electrode *(arrowheads)*. Note the excellent vessel conspicuity (*arrows* mark the sagittal superior sinus), which allows a safe intervention to be achieved without any bleeding complications. **d** Axial turbo spin-echo T2-weighted image (TR/TE/NSA/ETL: 2000/105 ms/2/17) confirms final RF electrode tip position *(white arrow)* before beginning interstitial thermotherapy

Fig. 2 Magnetic resonance-compatible manually driven 4.5-G titanium drill

(ROIs) on the MRI work station. The ROIs for signal intensity of tissue (RF thermal lesions and uninvolved contralateral frontal lobe) were at least 20 mm^2 and were chosen from homogeneous, artifact-free areas of the tissue being measured. The ROIs for noise were at least 500 mm^2 and were measured outside of the animal in the phase-encoding direction. Each signal amplitude value was calculated as the average of three, separately sampled ROIs. The brain-to-lesion contrast-to-noise ratio (CNR) was calculated for each sequence using Eq. (1) [16]:

$$CNR_{Brain\text{-}Lesion} = (SA_{Brain} - SA_{Lesion}) \div SA_{Noise}$$

where SA_{Brain}, SA_{Lesion}, and SA_{Noise} represent the signal amplitudes of the uninvolved contralateral frontal lobe, the RF thermal lesion, and the background noise, respectively.

Statistical analysis

Measurements of lesion diameter as determined by MRI were compared with measurements taken at gross pathology in terms of over- or underestimation, mean difference, minimum and maximum differences, and standard deviation. Furthermore, radiologic/pathologic correlation coefficients were calculated for each different sequence. The CNRs among various MR sequences were compared in terms of their minimum and maximum values, means, and standard deviations. Comparison of CNRs was performed with Student's *t*-test. A *p*-value less than 0.05 was considered to be significant.

Results

In all six procedures, the RF electrode was successfully placed without complications under MR guidance at the target site in the frontal lobe (Fig. 1). The time required to localize the skull insertion site with a fluid-filled syringe ranged from 2 to 8 min (4.7 ± 2.8 min). Following this step of the interventional procedure, drilling of the burr hole took place inside the MR gantry via the attached "open" head coil and never lasted longer than 3 min. The susceptibility artifact of the rotating titanium drill did not allow visualization of the dura during drill-

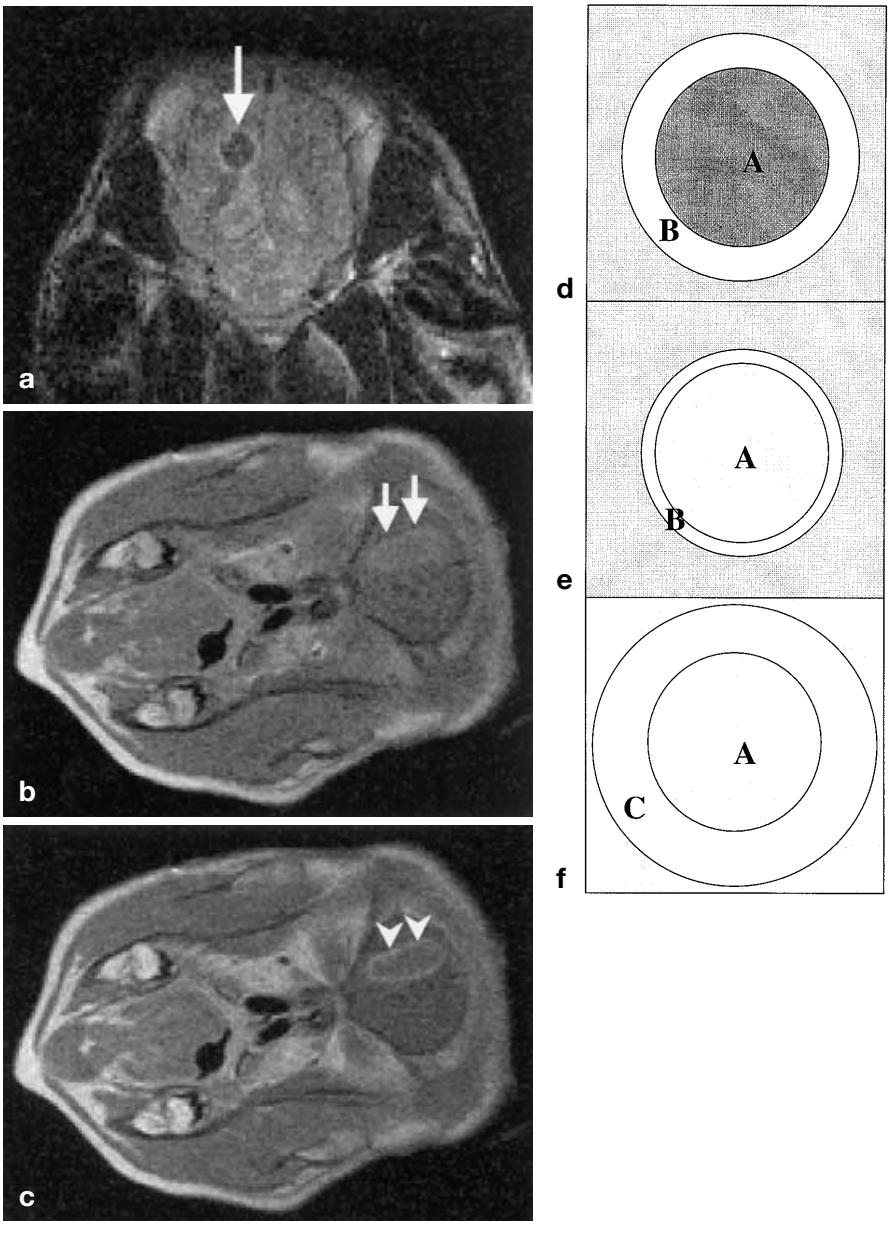

Fig. 3a–c The MR appearance of acute RF thermal lesion in the frontal lobe of porcine brain. **a** Coronal turbo spin-echo T2-weighted image (TR/TE/NSA/ETL: 2000/105 ms/2/17) acquired 1 min after RF ablation depicts an area of low signal intensity (zone A; *arrow*) in the frontal cerebral lobe surrounded by rim edema (zone B). **b** On unenhanced axial spin-echo T1-weighted imaging (TR/TE/NSA: 400/26 ms/3), the RF-induced lesion *(arrows)* appears hyperintense (zone A) compared with the contralateral frontal lobe. **c** On contrast-enhanced axial spin-echo T1-weighted imaging (TR/TE/NSA: 400/26 ms/3) using gadodiamide IV, the RF-induced lesion appears as a central hypointense nonenhancing zone (zone A) with rim enhancement (zone C; *arrowheads*)

ing of the burr hole; however, careful drilling through the internal osseous layer of the skull always protected the dura. The time required to place the electrode at the target site ranged from 2 to 7 min (4.8 ± 1.7 min) and included position confirmation with turbo spin-echo T2-weighted imaging. Overall, magnet time, from the first pre-procedure image until the last post-procedure image, ranged from 73 to 189 min, with a mean of 119 min.

Radiofrequency current during ablation averaged 412 ± 44 mA. The average current applied during the first minute of ablation was 438 ± 63 mA, whereas the average current during the tenth minute was 404 ± 36 mA.

Baseline impedance measured before RF application averaged 127 ± 9 Ω. The impedance dropped an average of 14.3 ± 5.5 Ω over the course of a 10-min ablation, and most of this impedance drop (12.0 ± 5.5 Ω) occurred during the first minute of ablation.

On immediate post-procedure imaging, RF thermal lesions demonstrated a typical pattern which consisted of three concentric zones (Fig. 3). The central area appeared dark on T2-weighted images and slightly hyperintense (compared with the contralateral frontal lobe) on unenhanced T1-weighted sequences in all cases (zone A). A small hyperintense rim regularly surrounded this zone on T2-weighted imaging (zone B). On post-gadolinium

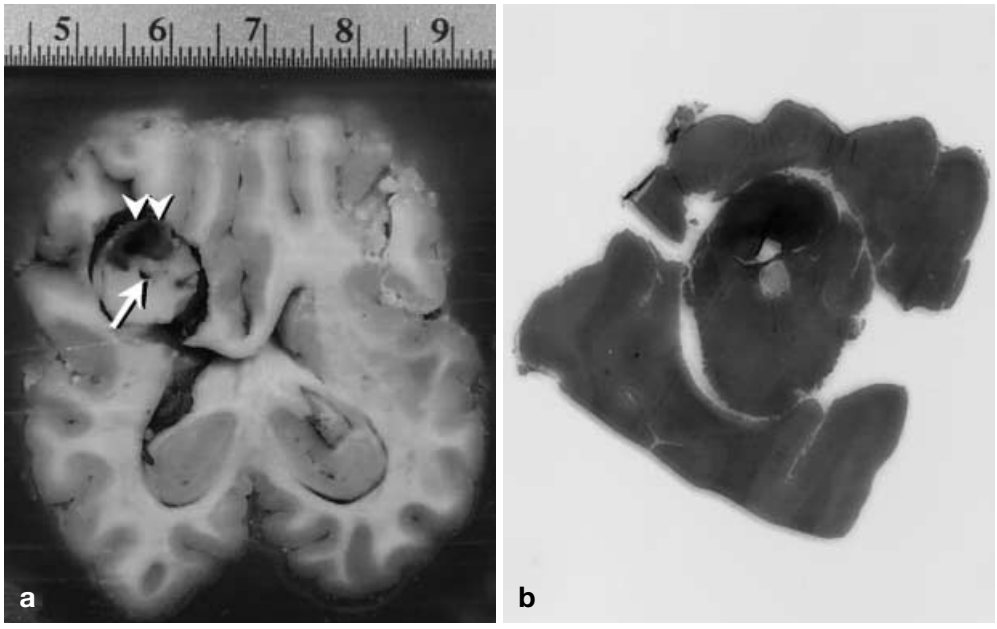

Fig. 4 a, b Gross brain specimen and microscopic depiction of acute RF thermal lesion. **a** The needle track *(arrow)* is clearly demarcated surrounded by a white, densely coagulative area representing the thermal lesion. Within this area, hemorrhage is seen *(arrowheads)*. **b** At histology (Masson's trichrome staining, 2 ×), the coagulative area is clearly depicted as well with sharp edges. The hemorrhage is also clearly visible

images, a peripheral enhancement outside of the rim area was visible (zone C). At gross examination, specimens demonstrated a target-like appearance which consisted of three distinct zones (Fig. 4 a). A zone of white, densely coagulated tissue surrounded a central hemorrhagic cavity. Grayish, depressed tissue with intermittent hemorrhage represented the third concentric zone. Microscopic examination revealed four distinct zones (Fig. 4 b). Three concentric zones surrounded a small central area of coagulated hemorrhagic necrosis. The innermost zone exhibited homogenization of the neuropil with preservation of cellular detail and engorgement of blood vessels. Edema and vacuolization of the neuropil characterized the next zone. Within this zone, small microhemorrhages in a concentric pattern were noted as a fourth area.

At gross pathologic analysis, coagulation, defined as a zone of white, densely coagulated tissue, varied from 10 to 12 mm (11 ± 1 mm). Turbo spin-echo T2-weighted images successfully demonstrated all six thermal lesions (Fig. 3). The maximum lesion diameter (zone A) on these images never exceeded that found at pathology (Table 1). The mean difference between the maximum lesion diameter on these images and the maximum lesion diameter found at pathology was 2.8 ± 1.2 mm (range 1–4 mm). The radiologic/pathologic correlation coefficient was 0.49. By including the surrounding rim edema (zones A + B), imaging overestimated pathologic lesion size in five of six cases with a mean difference of 2.2 ± 1.0 mm (range 1–3 mm) and a correlation coefficient of –0.47 (Table 1).

Unenhanced T1-weighted imaging demonstrated the thermal lesion in all six cases and always underestimated the maximum lesion diameter found at pathology (Fig. 3 b). The mean difference between imaged lesion

Table 1 Maximum diameter of radiofrequency (RF) thermal lesions perpendicular to the RF probe track as measured as various MR sequences (immediately post ablation) and at gross pathologic examination. All measurements are in millimeters. Difference represents the mean absolute difference between the imaged diameter and the pathologic diameter. Correlation represents the radiologic/pathologic correlation coefficient for the different sequences

Lesion	T2W Zone A	T2W Zones A + B	T1W Zone A	T1W + Gad Zone A	T1W + Gad Zones A + C	Pathology
1	8	11	7	10	15	12
2	8	12	7	8	12	11
3	7	13	9	7	13	10
4	6	12	6	7	11	10
5	8	13	6	9	13	10
6	14	14	10	10	14	11
Mean difference	2.8	2.2	3.2	2.2	2.3	
SD of difference	1.2	1.0	1.7	1.0	1.0	
Correlation	0.49	–0.47	0.15	0.71	0.69	

diameter and pathologic diameter was 3.2 ± 1.7 mm (range 1–5 mm) for this sequence with a radiologic/pathologic correlation of 0.15 (Table 1).

On contrast enhanced T1-weighted imaging, the maximum lesion diameter (zone A) regularly underestimated that found at pathology (Table 1). The mean difference between the maximum lesion diameter on these images and the maximum lesion diameter found at pathology was 2.2 ± 1.0 mm (range 1–3 mm) with a radiologic/pathologic correlation coefficient of 0.71. By including the surrounding hyperemia rim (zones A + C), imaging overestimated pathologic lesion size in all cases with a mean difference of 2.3 ± 1.0 mm (range 1–3 mm) and a correlation coefficient of 0.69 (Table 1).

Gadolinium-enhanced T1-weighted imaging demonstrated the most contrast between lesion and uninvolved contralateral brain, with an average CNR of 1.5 ± 1.6 (range 0.3–4.7, based on absolute CNR values). Unenhanced T1-weighted images demonstrated the least contrast, with an average CNR of 0.7 ± 0.5 (range 0.1–1.4). T2-weighted images had an average CNR of 1.1 ± 1.0 (range 0.1–2.6). On Student's *t*-test, no statistically significant differences were observed (T2-weighted vs unenhanced T1-weighted: $p = 0.52$; unenhanced T1-weighted vs enhanced T1-weighted: $p = 0.20$; T2-weighted vs enhanced T1-weighted: $p = 0.63$).

Discussion

The estimated number of new cases of primary cancer in the human nervous system in the United States in 1998 was 9800 for men and 7600 for women [17]. The estimated number of cancer deaths during the same time period was 7300 for men and 6000 for women, reflecting the poor prognosis for this type of cancer. Furthermore, the brain is a common site for secondary neoplasms. In the past, surgical resection was the only curative treatment modality. Its main disadvantage is the damage to uninvolved brain tissue, especially if a long access path is required for deeply located lesions. External beam radiotherapy was used as a supporting treatment modality or as an alternative option for palliative management. During the past decade, gamma-knife radiosurgery was established as a potentially curative, minimally invasive treatment modality for focal brain lesions [18]. The disadvantage of radiotherapy, however, is the delayed tumor response and its lack of repeatability due to cumulative dose effects.

Percutaneous RF ablation is a safe, minimally invasive modality which has been used in stereotactic neurosurgical procedures for more than 30 years [19]. Since the late 1980s, RF-induced tumor ablation has also been used in early clinical trials for treatment of hepatocellular carcinoma [20], hepatic [21, 22, 23], and cerebral metastases [7], and benign bony lesions such as osteoid osteomas [24]. Typically, under cross-sectional imaging guidance, a thin (usually 14–21 G) electrode is placed percutaneously directly into the tumor. Coagulation necrosis results from resistive heating in the tissue adjacent to the non-insulated part of the electrode.

A modern imaging and guidance modality for minimally ablative tumor treatment should fulfill two conditions: Firstly, insertion of the RF electrode into the tumor should be possible in a safe and rapid manner. Magnetic resonance imaging, with its high soft tissue contrast, multiplanar imaging capabilities, high spatial resolution, and ability to visualize the vessels without administration of contrast medium, seems to be well suited for target definition and trajectory selection [25]. The development of open MR scanners with wide patient access now also allows RF electrode insertion and tracking under MR fluoroscopy [26, 27]. In some aspects, the brain is an anatomically favored site for interstitial thermotherapy, because it most often gives rise to unifocal neoplasms. However, the most serious shortcoming of MR-guided thermal ablative treatment of malignant brain tumors is an underlying lack of precise target definition; this is also true for gamma-knife radiosurgery. The surgical "assumption" of a well-defined tumor mass is incorrect, and spatially disseminated tumor cells may spread beyond the reach of the thermal treatment. Nevertheless, if a cure is not anticipated, a less invasive procedure is increasingly justified for palliation [5].

Secondly, and of even more importance, is the necessity for control of destructive RF energy deposition. This is most important in the brain where thermal damage must be limited to the target lesion to exclude damage to sensitive structures [5]. Jolesz postulated a two-fold role for MR monitoring of thermal ablative treatment [5]. Firstly, real-time MR imaging with temperature-sensitive pulse sequences can display transient temperature elevations [9, 28]. This allows the interventional clinician to confine thermal treatment to the target tissue, thus preventing damage to surrounding structures. The second role of MR imaging is to delineate the irreversible tissue necrosis. Similar to its application in the liver [14], its ability to visualize the resulting thermal lesion intraoperatively, but immediately after the first MR image-guided thermotherapy procedure (with the RF electrode still in place), provides the opportunity to reposition the RF electrode and repeat the ablation in order to ensure that all targeted tissue and margin have been adequately treated.

Using low-field MR guidance, we were able to access the desired insertion site in the cerebral frontal lobe without difficulty using the 18-G RF electrode in all six pigs in our series. Excellent vessel conspicuity, due to flow-related enhancement effects inherent in 2D Fourier transform gradient-echo sequences used for electrode guidance, enabled us to achieve a safe intervention

without any complications (Figs. 1 b,c). This is in contradiction to the previously published clinical studies in which a stereotactic guidance system was used for electrode insertion.

The total magnet time ranged from 1 to 3 h with a mean of 2 h. This time included the prescan, localization and drilling of the burr hole, RF electrode insertion using gradient-echo sequences, confirmation of the electrode tip using turbo spin-echo T2-weighted imaging, the RF ablation procedure itself, and the multiplanar postscan with and without contrast enhancement. These data concerning time consumption were encouraging to us and demonstrate not only the feasibility of this approach, but also its reasonable length of time.

Low-field MR imaging also allowed monitoring of the RF ablation procedure itself. The gross pathologic and histologic appearance of acute heat-induced lesions in the brain as well as their high field MR imaging counterparts are well known and have been described in the literature [8, 10, 29, 30, 31]. Generalized damage of cellular and subcellular membranes is observed with empty-appearing intravascular red blood cells in the central zone [25, 30]. Sometimes, an innermost high signal intensity is visible, most likely representing heat-induced methemoglobin conversion from deoxyhemoglobin, which normally takes more than 72 h in an intracranial hematoma without heat induction [7]. This area represents a small amount of local bleeding caused by electrode insertion. The outermost zone reveals no membrane disruptions but rather edema with generalized swelling and the empty appearance of nerve cell processes and astrocytic foot processes [25, 30].

On low-field MR imaging, RF-induced thermal lesions could be clearly identified immediately after the procedure (Fig. 3), but only demonstrated three different zones. The thermal lesions appeared as hypointense regions on T2-weighted (zone A) images and were surrounded by peripheral hyperintense areas suggestive of edema (zone B; Fig. 3 a,d). On T1-weighted sequences, RF-induced lesions were slightly hyperintense (zone A; Fig. 3 b,e) but better depicted after gadodiamide administration when they appeared as central hypointense nonenhancing areas with peripheral rim enhancement (zone C; Fig. 3 c,f). Calculated brain-to-RF-induced lesion CNRs were highest for contrast-enhanced T1-weighted images, but these values were not significantly different from those of unenhanced spin-echo T1-weighted and turbo spin-echo T2-weighted images.

Using high-field MRI for monitoring the ablation process, the acute thermal lesion consists of four concentric zones with reverse signal intensities on T1-weighted vs T2-weighted images [25]. In addition to the three concentric zones described previously for low-field MR monitoring, a low signal intensity rim on T2-weighted images is visible as a fourth concentric zone and most likely represents deoxyhemoglobin in the acute stage [7]. This area also demonstrates enhancement following gadolinium-containing contrast medium administration. This discrepancy between low- and high-field MR imaging might represent a true effect of field strength caused by the increased signal-to-noise ratio and a greater temporal resolution of the high-field studies. Another possible explanation relates to the size of the thermal lesion in our investigation. The four-zone architecture of thermal lesions was found in human trials with a brain size of approximately 10 cm and thermal lesion size of up to 3 cm perpendicular to the electrode track, as compared with the porcine brain size of only 5 cm and lesion size of 10–12 mm in our investigation. Anzai et al. [7] noted that this additional fourth zone was not seen during treatment of small tumors less than 1 cm in diameter, further suggesting that the absence of this zone in our study may be lesion-size related.

Thermal lesion size in our study, which ranged from 10 to 12 mm on gross pathology perpendicular to the electrode track, might not be of sufficient size for adequate tumor treatment in many instances in clinical practice. In the liver, the diameter of coagulation can be increased to approximately 24 mm [32] perpendicular to the electrode track without repositioning the device if technically modified perfused RF systems developed to increase energy deposition into the tissue are used. It is reasonable to expect that an increase in maximal lesion diameter could be achieved in the brain if perfused RF systems were applied, thereby allowing creation of somewhat larger thermal lesions at each electrode position during interstitial thermal treatment. Lesion diameter along the electrode track is predetermined by the electrode design and is closely related to the length of the non-insulated segment of the electrode tip [33] but can easily be increased by slightly withdrawing the electrode and repeating the RF application.

Contrast-enhanced axial spin-echo T1-weighted imaging acquired immediately after intervention slightly underestimated the pathologic diameter of the thermal lesion in all cases, if only zone A was considered as the thermal lesion. On the other hand, gadodiamide enhanced T1-weighted imaging regularly overestimated the pathologic diameter with a mean difference between radiologic and pathologic measurements of RF lesion diameter of 2.3 ± 1.0 mm (Table 1) if the hyperemic rim (zone C) was included in the measurements. This slight error in predicting lesion size, although never more than 3 mm, may be a true manifestation of the MR imaging technique. However, it may also reflect the mild tissue shrinkage which may occur with pathological fixation. Another explanation of this slight error may be the alteration of thermal lesion size over time. It is known that thermal lesion size may increase within several days due to delayed heat effects, e. g., Schwabe et al. [25] reported an increase of the total size of laser-induced thermal lesions in the human brain by 23 % in

average within the first 10 days. Transferring these results to our study would lead to an even better correlation of gadodiamide enhanced T1-weighted imaging and pathology. Differentiation between these possibilities, however, will require further investigation with more advanced pathologic techniques, such as the use of fiducial markers [34]. Another option for monitoring the thermal ablation process is turbo spin-echo T2-weighted imaging which requires approximately 1 min and always underestimates pathologic thermal lesion size. A practical approach could be the use of T2-weighted images for monitoring the irreversible tissue necrosis by considering only "zone A" the thermal lesion area. This method would always underestimate real pathologic lesion size, and thus, if the area of hypointensity was tailored to include the entire tumor, would result in a small rim of treated tissue surrounding the tumor. After repositioning the RF electrode (if needed) and re-ablation (in the same treatment session), the final post-procedure imaging could be performed using T1-weighted images with and without gadolinium enhancement.

Until recently, the significant interference between RF generators and MR imagers has prevented simultaneous imaging and RF ablation. This has been overcome by the development of a simple switching circuit which now provides compatibility between open MRI systems and RF thermal lesion generators [35]. This allows online temperature mapping during the interventional procedure, which is now also available for mid-field and low-field systems [28, 36]. These sequences are based on gradient-echo techniques, and the fact that the susceptibility artifact size of the 18-G titanium RF electrode used in this study is nearly 10 mm in diameter on gradient-echo imaging, thus obscuring the temperature map in the region of interest; therefore, no temperature monitoring was performed in our study.

In conclusion, we accept the hypothesis that low-field MR image-guided RF thermal ablation in the brain is feasible in a porcine model and reasonable in terms of the time required. Induced thermal lesion size can best be monitored using T2-weighted and enhanced T1-weighted images acquired immediately after intervention, thereby allowing feedback and, when necessary, repositioning of the RF electrode. Radiofrequency ablation may offer an alternative future treatment option for primary and secondary brain neoplasms, perhaps by becoming part of a multimodal therapeutic strategy.

Acknowledgements The authors thank V. Wong, Department of Surgery of University Hospitals of Cleveland/Case Western Reserve University, for her invaluable assistance in dissecting the animals; K. Corcoran and T. McCourt for assistance in animal observation and anesthesia; M. Wendt for helpful conversations; E. DuPont and B. Hami for assistance in manuscript preparation; and all of the members of Interventional MR Research. This work was supported in part by grants from The Whitaker Foundation, Siemens Medical Systems, Minrad Inc., Radionics, American Cancer Society, Mary Ann S. Swetland Fund, M.E. and F.J. Callahan Foundation, and the "Deutsche Forschungsgemeinschaft" (grant no. Me 1593/1–1)

References

1. Kahn T, Bettag M, Ulrich F, Schwarzmaier HJ, Schober R, Furst G, Modder U (1994) MRI-guided laser-induced interstitial thermotherapy of cerebral neoplasms. J Comput Assist Tomogr 18: 519–532
2. Gilbert JC, Rubinsky B, Roos MS, Wong ST, Brennan KM (1993) MRI-monitored cryosurgery in the rabbit brain. Magn Reson Imaging 11: 1155–1164
3. DeSalles AA, Brekhus SD, Souza EC de, Behnke EJ, Farahani K, Anzai Y, Lufkin R (1995) Early postoperative appearance of radiofrequency lesions on magnetic resonance imaging. Neurosurgery 36: 932–936
4. McDannold NJ, Hynynen K, Wolf D, Wolf G, Jolesz F (1998) MRI evaluation of thermal ablation of tumors with focused ultrasound. J Magn Reson Imaging 8: 91–100
5. Jolesz FA (1995) MR-guided thermal ablation of brain tumors. Am J Neuroradiol 16: 49–52
6. Moriarty JA, Chen JC, Purcell CM, Ang LC, Hinks RS, Peters RD, Henkelman RM, Plewes DB, Bronskill MJ, Kucharczyk W (1998) MRI monitoring of interstitial microwave-induced heating and thermal lesions in rabbit brain in vivo. J Magn Reson Imaging 8: 128–135
7. Anzai Y, Lufkin R, DeSalles A, Hamilton DR, Farahani K, Black KL (1995) Preliminary experience with MR-guided thermal ablation of brain tumors. Am J Neuroradiol 16: 39–48
8. Tracz RA, Wyman DR, Little PB, Towner RA, Stewart WA, Schatz SW, Wilson BC, Pennock PW, Janzen EG (1993) Comparison of magnetic resonance images and the histopathological findings of lesions induced by interstitial laser photocoagulation in the brain. Laser Surg Med 13: 45–54
9. Kahn T, Harth T, Kiwit JC, Schwarzmaier HJ, Wald C, Modder U (1998) In vivo MRI thermometry using a phase-sensitive sequence: preliminary experience during MRI-guided laser-induced interstitial thermotherapy of brain tumors. J Magn Reson Imaging 8: 160–164
10. Schulze CP, Kahn T, Harth T, Schwurzmaier HJ, Schober R (1998) Correlation of neuropathologic findings and phase-based MRI temperature maps in experimental laser-induced interstitial thermotherapy. J Magn Reson Imaging 8: 115–120
11. Fan M, Ascher PW, Schröttner O, Ebner F, Germann RH, Kleinert R (1992) Interstitial 1.06 Nd: YAG Laser thermotherapy for brain tumors under real-time monitoring of MRI: experimental study and phase I clinical trial. J Clin Laser Med Surg 10: 355–361

12. Lewin JS, Petersilge CA, Hatem SF, Duerk JL, Lenz G, Clampitt ME, Williams ML, Kaczynski KR, Lanzieri CF, Wise AL, Haaga JR (1998) Interactive MR imaging-guided biopsy and aspiration with a modified clinical C-arm system. Am J Roentgenol 170: 1593–1601
13. Lewin JS, Duerk JL, Jain VR, Petersilge CA, Chao CP, Haaga JR (1996) Needle localization in MR-guided biopsy and aspiration: effects of field strength, sequence design, and magnetic field orientation. Am J Roentgenol 166: 1337–1345
14. Lewin JS, Connell CF, Duerk JL, Chung YC, Clampitt ME, Spisak J, Gazelle GS, Haaga JR (1998) Interactive MRI-guided radiofrequency interstitial thermal ablation of abdominal tumors: clinical trial for evaluation of safety and feasibility. J Magn Reson Imaging 8: 40–47
15. Boaz TL, Lewin JS, Chung YC, Duerk JL, Clampitt ME, Haaga JR (1998) MR monitoring of MR-guided radiofrequency thermal ablation of normal liver in an animal model. J Magn Reson Imaging 8: 64–69
16. Ros PR, Freeny PC, Harms SE, Seltzer SE, Davis PL, Chan TW, Stillman AE, Muroff LR, Runge VM, Nissenbaum MA (1995) Hepatic MR imaging with ferumoxides: a multicenter clinical trial of the safety and efficacy in the detection of focal hepatic lesions. Radiology 196: 481–488
17. Landis SH, Murray T, Bolden S, Wingo PA (1998) Cancer statistics, 1998. CA Cancer J Clin 48: 6–29
18. Kawana K, Yoshikawa H, Yokota H, Onda T, Nakagawa K, Tsutsumi O, Taketani Y (1997) Successful treatment of brain metastases from ovarian cancer using gamma-knife radiosurgery. Gynecol Oncol 65: 357–359
19. Brodkey JS, Miyazaki Y, Ervin FR, Mark VH (1964) Reversible heat lesions with radio frequency current: a method of stereotactic localization. J Neurosurg 21: 49–53
20. Rossi S, Di SM, Buscarini E, Quaretti P, Garbagnati F, Squassante L, Paties CT, Silverman DE, Buscarini L (1996) Percutaneous RF interstitial thermal ablation in the treatment of hepatic cancer. Am J Roentgenol 167: 759–768
21. Solbiati L, Ierace T, Goldberg SN, Sironi S, Livraghi T, Fiocca R, Servadio G, Rizzatto G, Mueller PR, Del MA, Gazelle GS (1997) Percutaneous US-guided radio-frequency tissue ablation of liver metastases: treatment and follow-up in 16 patients. Radiology 202: 195–203
22. Livraghi T, Goldberg SN, Monti F, Bizzini A, Lazzaroni S, Meloni F, Pellicano S, Solbiati L, Gazelle GS (1997) Saline-enhanced radio-frequency tissue ablation in the treatment of liver metastases. Radiology 202: 205–210
23. Solbiati L, Goldberg SN, Ierace T, Livraghi T, Meloni F, Dellanoce M, Sironi S, Gazelle GS (1997) Hepatic metastases: percutaneous radio-frequency ablation with cooled- tip electrodes. Radiology 205: 367–373
24. Rosenthal DI, Springfield DS, Gebhardt MC, Rosenberg AE, Mankin HJ (1995) Osteoid osteoma: percutaneous radio-frequency ablation. Radiology 197: 451–454
25. Schwabe B, Kahn T, Harth T, Ulrich F, Schwarzmaier HJ (1997) Laser-induced thermal lesions in the human brain: short- and long-term appearance on MRI. J Comput Assist Tomogr 21: 818–825
26. Silverman SG, Collick BD, Figueira MR, Khorasani R, Adams DF, Newman RW, Topulos GP, Jolesz FA (1995) Interactive MR-guided biopsy in an open-configuration MR imaging system. Radiology 197: 175–181
27. Silverman SG, Jolesz FA, Newman RW, Morrison PR, Kanan AR, Kikinis R, Schwartz RB, Hsu L, Koran SJ, Topulos GP (1997) Design and implementation of an interventional MR imaging suite. Am J Roentgenol 168: 1465–1471
28. Steiner P, Botnar R, Dubno B, Zimmermann GG, Gazelle GS, Debatin JF (1998) Radio-frequency-induced thermoablation: monitoring with T1-weighted and proton-frequency-shift MR imaging in an interventional 0.5-T environment. Radiology 206: 803–810
29. Farahani K, Mischel PS, Black KL, De SA, Anzai Y, Lufkin RB (1995) Hyperacute thermal lesions: MR imaging evaluation of development in the brain. Radiology 196: 517–520
30. Schober R, Bettag M, Sabel M, Ulrich F, Hessel S (1993) Fine structure of zonal changes in experimental Nd:YAG laser-induced interstitial hyperthermia. Laser Surg Med 13: 234–241
31. Tracz RA, Wyman DR, Little PB, Towner RA, Stewart WA, Schatz SW, Pennock PW, Wilson BC (1992) Magnetic resonance imaging of interstitial laser photocoagulation in brain. Laser Surg Med 12: 165–173
32. Goldberg SN, Gazelle GS, Solbiati L, Rittman WJ, Mueller PR (1996) Radiofrequency tissue ablation: increased lesion diameter with a perfusion electrode. Acad Radiol 3: 636–644
33. Goldberg SN, Gazelle GS, Dawson SL, Rittman WJ, Mueller PR, Rosenthal DI (1995) Tissue ablation with radiofrequency: effect of probe size, gauge, duration, and temperature on lesion volume. Acad Radiol 2: 399–404
34. Morrison PR, Jolesz FA, Charous D, Mulkern RV, Hushek SG, Margolis R, Fried MP (1998) MRI of laser-induced interstitial thermal injury in an in vivo animal liver model with histologic correlation. J Magn Reson Imaging 8: 57–63
35. Zhang Q, Chung YC, Lewin JS, Duerk JL (1998) A method for simultaneous RF ablation and MRI. J Magn Reson Imaging 8: 110–114
36. Chung YC, Duerk JL, Shankaranarayanan A, Hampke M, Merkle EM, Lewin JS (1999) Temperature measurement using echo-shifted FLASH at low field for interventional MRI. J Magn Reson Imaging 9: 138–145